



Final Draft of the original manuscript

Raza, S.; Klusemann, B.:

Multiphase-field modeling of temperature-driven intermetallic compound evolution in an Al-Mg system for application to solid-state joining processes.

In: Modelling and Simulation in Materials Science Engineering.
Vol. 28 (2020) 8, 085003.

First published online by IOP: 02.07.2020

<https://dx.doi.org/10.1088/1361-651X/aba1df>

Multiphase-field modeling of temperature-driven intermetallic compound evolution in an Al-Mg system for application to solid-state joining processes

Syed Hasan Raza¹, Benjamin Klusemann^{1,2}

¹ Institute of Product and Process Innovation, Leuphana University of Lüneburg, Lüneburg, Germany

² Institute of Materials Research, Materials Mechanics, Solid State Joining Processes, Helmholtz-Zentrum Geesthacht, Geesthacht, Germany

E-mail: raza@leuphana.de

March 2020

Abstract. Solid-state joining of dissimilar materials results typically in the formation of intermetallic compounds at the weld interface, which strongly determines the resulting mechanical properties. To tailor the joint strength, understanding of the formation of the intermetallic compound and their driving mechanisms is crucial. In this study, the evolution of temperature-driven Al_3Mg_2 and $\text{Al}_{12}\text{Mg}_{17}$ intermetallic compounds in an Al-Mg system for application to solid-state joining processes via a multiphase-field approach is numerically investigated. To this end, the CALPHAD approach to obtain the thermodynamic parameters of the relevant phases is used in conjunction with the multiphase-field model. The simulation results are qualitatively compared with experimental results in the literature in terms of thickness and morphology of intermetallic grains, exhibiting a reasonable agreement. The influence of grain boundary diffusion and interface energy on the morphology and kinetics of the intermetallic compound grains is investigated in detail with the established multiphase-field model.

Keywords: multiphase-field modeling, intermetallic compound, Al-Mg system, solid-state joining processes Submitted to: *Modelling Simul. Mater. Sci. Eng.*

1. Introduction

With an estimation of over 40,000 metallic alloys [1], the production of metals and alloys is quite impressive, to say the least. Understanding the physical phenomenon during the processing and joining of materials is vital for producing and controlling the microstructure of the material in order to optimize the properties. In particular,

Aluminum (Al) and Magnesium (Mg) alloys are highly relevant materials for the transport industry because of their excellent strength to weight ratios [2], resulting in the prospect of multi-material structures consisting of the two alloys as an attractive research field [3]. There have been many attempts to join these alloys via traditional fusion welding techniques, however, the obtained welds via such techniques exhibit inferior performance concerning the formation of excessive brittle intermetallic phases at the interface [4, 5]. The inherent nature of such intermetallic compounds and their formation at the interface, may lead to poor mechanical properties of the obtained joint [6, 4].

In contrast to fusion-based joining processes, solid-state joining processes bonds two materials in solid-state, allowing the possibility of obtaining a defect-free weld with superior properties. Joining in solid-state avoids metallurgical reactions taking place at melting and solidification, avoiding the formation of pores. Furthermore, the temperatures reached during solid-state joining are lower than the ones obtained in the fusion-based welding processes, i.e. at most 80% of the melting temperature, resulting in controlled intermetallic compound growth [2, 7].

An example of a solid-state joining process represents the refill Friction Stir Spot Welding process (refill FSSW) [8, 9] where two materials are joined based on diffusion expedited by frictional heating and severe plastic deformation. The FSSW process is mature and applied for the joining of similar materials [10, 11, 12, 13, 14] as well as dissimilar materials [15, 16, 17, 18]. During the joining of dissimilar materials, intermetallic compounds tend to form at the interface, which affect the weld strength. Suhuddin et al. [19] joined Al/Mg alloys and studied the formation and evolution of Al_3Mg_2 and $\text{Al}_{12}\text{Mg}_{17}$ intermetallic compounds. The authors found a reduction in the lap shear strength of the joints due to the distribution of the intermetallic compounds. It was also concluded that the driving force for the intermetallic phases at the weld interface is not just temperature but also excessive plastic deformation. Furthermore, the severe plastic deformation also enhances the diffusion rate, potentially leading to higher growth of intermetallic compounds in contrast to the case where plastic deformation is absent. Zettler et al. [20] and Khodir et al. [21] also observed the formation of Al_3Mg_2 and $\text{Al}_{12}\text{Mg}_{17}$ intermetallic compounds during FSSW of Al to Mg. Plaine et al. [22] produced FSSW welds of Al/Ti alloys and investigated, among other things, the formation of TiAl_3 intermetallic compounds and their influence on the joint strength. To produce engineering quality welds, understanding the evolution and the driving mechanisms of such intermetallic compounds is essential [6].

To this end, for the investigation of microstructure evolution, multiphase-field methods are currently one of the widely used approaches [23]. The use of the multiphase-field method potentially allows to compute temporal and spatial microstructural evolution along with the associated kinetics of intermetallic compounds based on the diffuse interface. The strength of the method is the use of a single function to describe the evolution of the phase-field regardless of the number of domains and thus allowing not to keep track of the interface explicitly [24]. Multiphase-field methods

treat the microstructural evolution (in terms of compositional/structural domains along with the interfaces [25]) with the help of a set of phase-field variables, which are a function of space and time [26]. There are two kinds of field variables: conserved and non-conserved, where the distinction is based on whether the variable is being conserved i.e. satisfying local conservation condition [25] or not. Conserved variables are typically related to local composition in terms of molar fractions or concentration. Non-conserved variables can be distinguished either as order parameters or phase-fields. Order parameters represent local (crystal) structure and orientation, while phase-fields are phenomenological variables in nature which indicate the presence of a certain phase (or grain) [26]. Phase-field variables represent a property of a system that is non-zero in a distinct region and zero otherwise, i.e. a distinction between two states such as solid/liquid or two grains. In a multiphase system, the sum of the order parameters for all phases is thus one [23]. The interface represents the region where the phase-field variables vary. In the phase-field method, multiple driving forces responsible for microstructural evolution can be considered while formulating the total free energy function and thus different phase-field models for various applications differ from each other based on their treatment of the different energy contributions to the total free energy. The total free energy is described via the field variables and their gradients [24]. For a more qualitative analysis, Landau polynomial expressions [27] are sometimes used for the representation of the free energy, whereas CALPHAD [28] can be coupled with the phase-field method for quantitative analysis [29]. Temporal microstructure evolution is described by the Cahn-Hilliard nonlinear diffusion continuum equation [30], describing the evolution of composition-fields and the Allen-Cahn (time-dependent Ginzburg-Landau) equation, describing the evolution of phase-fields [25].

Regarded as “FEM for metallurgists and materials scientists” by Schmitz et al. [31], multiphase-field methods have been successfully implemented in the field of solidification [32, 33, 34], grain growth [35, 36], fracture mechanics [37, 38], along with solid-state phase transformations [39, 40, 41]. Zhang et al. [42] applied the multiphase-field method for the prediction of the interdiffusion microstructure in Ni-Al diffusion couples. Takaki et al. [43] coupled a multiphase-field method with a finite-element based crystal plasticity approach for the simulation of static recrystallization. With regard to intermetallics, Park et al. [44, 45, 46], Li et al. [47], Umantsev [48], and Huh et al. [49] focused on intermetallic compound evolution during soldering of Cu-Sn system. Hou et al. [50] simulated the process of intermetallic compounds during the precipitation process in a Ni-Al alloy system. Wang et al. [51] proposed a phase-field kinetic model for the simulation of precipitation of ordered intermetallics in a face-centered cubic solid solution of Ni-Al system. Recently, Welland et al. [29] developed a method to couple CALPHAD with a phase-field model based on a grand-potential functional [52] rather than free energy functional [53] for the case of intermetallic growth in Al-Mg system. However, there have been very few studies related to the intermetallic compound evolution with reference to solid-state joining processes for dissimilar materials such as Al and Mg.

Motivated by solid-state joining processes, this study presents a multiphase-field approach to investigate temperature-driven intermetallic compound evolution in an Al/Mg weld. This is the first step to understand the evolution of intermetallic compounds during processes like FSSW, where additional contributions such as severe plastic deformation further need to be considered. The structure of this paper is as follows: In Section 2, a theoretical background of the multiphase-field approach along with the required parameters, in particular, the calculation of chemical-free energy via the CALPHAD approach, is presented. In Section 3, the implementation of the multiphase-field approach for the selected case of the FSSW process for Al and Mg is discussed. Setup of the initial microstructure consisting of four phases, namely Al, Al_3Mg_2 , $\text{Al}_{12}\text{Mg}_{17}$, and Mg, along with the numerical implementation of the approach and its algorithm are parts of the section. Section 4 exhibits the capability of this model to simulate the evolution of the intermetallic compounds via two-dimensional multiphase-field simulations. Finally, Section 5 concludes the approach and findings of this contribution.

2. Theory

2.1. Multiphase-field model

Let \ddagger $\phi_i(\mathbf{x}, t)$, for $i = 1, \dots, N$, be the non-conserved field variable to represent the spatial distribution \mathbf{x} of each phase i at time t , where N represents the total number of phase-field variables, and $c_i(\mathbf{x}, t)$, for $i = 1, \dots, N$, be the conserved field variable denoting the spatial composition of each phase i at time t . The phase-field variable ϕ_i can be considered as the local fraction of the phase (or grain) designated by the subscript. The phase-field and the composition-field variables are subjected to the following constraints at any position in the system

$$\sum_{i=1}^N \phi_i(\mathbf{x}, t) = 1, \quad (1)$$

$$\sum_{i=1}^N \phi_i(\mathbf{x}, t) c_i(\mathbf{x}, t) = c(\mathbf{x}, t), \quad (2)$$

respectively. (1) ensures that the sum of all the phase-field variables equals one even though each phase-field variable varies between zero and one at the interfaces (and grain boundaries). (2) subjects the phase composition of the coexisting phases c_i to the local

\ddagger The following notation is used: Definitions are denoted by $:=$. Assuming a, b, c , and d as scalars, and \mathbf{e} and \mathbf{f} as vectors, $c = a \cdot b$ and $d = \mathbf{e} \cdot \mathbf{f}$ represent the dot product. $\nabla(\bullet)$ designates the gradient operator and $\ln(\bullet)$ represents the natural logarithm. $\dot{\bullet}$ represents time derivative, whereas \bullet^x represents the derivative of \bullet with respect to x and $\bullet^{x,y}$ represents the second derivative of \bullet with respect to x and y , i.e. $\bullet^{x,y} = \frac{\partial^2 \bullet}{\partial x \partial y}$. Square brackets $[\dots]$ are used to collect mathematical expressions and components in explicit vector and matrix representations whereas round brackets (\dots) represent function arguments.

mass conservation condition. The total free energy F of a heterogeneous system as a function of each phase is given as [44, 45, 46, 49]

$$F(\phi_i(\mathbf{x}, t), c(\mathbf{x}, t)) = \int_{\mathbf{v}} \left[\sum_{i=1}^N \phi_i f_i(c_i) + \sum_{j=1, j \neq i}^N \sum_{i=1}^N \left[-\frac{\epsilon_{ij}^2}{2} \nabla \phi_i \cdot \nabla \phi_j + \omega_{ij} \phi_i \phi_j \right] + \lambda_{\phi} \left[\sum_{i=1}^N \phi_i - 1 \right] \right] dV, \quad (3)$$

where f_i is the chemical free energy density of the i -th phase as a function of its composition c_i , ϵ_{ij} is the gradient energy coefficient corresponding to the energy barrier of i -th and j -th phase interface. ω_{ij} denotes the energy barrier for the transformation from ϕ_i to ϕ_j . Since only the values between $0 \leq \phi_i \leq 1$ have a physical meaning, the “double obstacle” potential $\phi_i \phi_j$ is bounded to ∞ for $\phi_i > 1$ ($\phi_j < 0$) or $\phi_i < 0$ ($\phi_j > 1$), allowing the computation of evolution of phase-field variables only for the well-defined, finite region of the interface [54, 49]. λ_{ϕ} in (3) is the Lagrangian multiplier and is used to enforce the constraint formulated by (1).

The solution of Cahn-Hilliard and Allen-Cahn equations lead to obtaining the evolution of the composition- and phase-fields, respectively. The Cahn-Hilliard equation is given by:

$$\dot{c}_i = -\nabla \cdot \mathbf{j}_i, \quad (4)$$

where \mathbf{j}_i is the flux determined via

$$\mathbf{j}_i = -M_c(c, \phi_i) \nabla \left(\frac{\delta F}{\delta c_i} \right), \quad (5)$$

where $M_c(c, \phi_i)$ is the atomic mobility and $\frac{\delta F}{\delta c_i}$ is the variational derivative of the free energy function with respect to the composition-field variable. Since the interface region represents the mixture of different phases, the coexisting phases at a position in the interface region are assumed to have an identical diffusion potential, for the sake of simplicity§ [56, 44]. The diffusion potentials are defined as the derivative of chemical free energy with respect to chemical composition of constituents species

$$\frac{\partial f_1}{\partial c_1} = \frac{\partial f_2}{\partial c_2} = \dots = \frac{\partial f_N}{\partial c_N} \equiv f^c(c, \phi_i), \quad (6)$$

indicating that the compositions of the coexisting phases at a given point are not independent of each other but constrained by the condition in (6). The variational

§ Alternatively it could be assumed that the coexisting phases at a point have an equal composition, i.e. $c_1(\mathbf{x}, t) = c_2(\mathbf{x}, t) = \dots = c_N(\mathbf{x}, t) \equiv c$. With the imposed equal diffusion potential condition instead of equal concentration condition, the extra chemical double-well potential at the interfacial region can be avoided [55]. As per the free energy densities curve, the equal diffusion potential represents the common tangent between two free energy curves (i.e. the extra potential is not considered) whereas equal concentration assumption, by definition, leads to extra double-well potential in the free energy description at the interface.

derivative in (5) can thus be computed as

$$\frac{\delta F}{\delta c} = \sum_{i=1}^N \phi_i \left[\frac{\partial f_i}{\partial c_i} \right] \left[\frac{\partial c_i}{\partial c} \right] = f^c(c, \phi_i), \quad (7)$$

since (2) can be reduced to

$$\sum_{i=1}^N \phi_i \left[\frac{\partial c_i}{\partial c} \right] = 1. \quad (8)$$

Introducing the interdiffusion coefficient D as a function of atomic mobility such that $M_c = \frac{D}{f^{c,c}}$ and considering that $\frac{f^{c,\phi_i}}{f^{c,c}} = -c_i$, the Cahn-Hilliard equation, (4), can be written as

$$\begin{aligned} \dot{c} &= \nabla \cdot \frac{D}{f^{c,c}} \nabla f^c, \\ &= \nabla \cdot D \nabla c + \nabla \cdot \frac{D}{f^{c,c}} \sum_{i=1}^N f^{c,\phi_i} \nabla \phi_i, \\ &= \nabla \cdot D \nabla c - \nabla \cdot D \sum_{i=1}^N c_i \nabla \phi_i, \\ &= \nabla \cdot D \left[\nabla c - \sum_{i=1}^N c_i \nabla \phi_i \right], \\ \dot{c} &= \nabla \cdot \left[D \sum_{i=1}^N \phi_i \nabla c_i \right], \end{aligned} \quad (9)$$

since (2) leads to

$$\nabla c(\mathbf{x}, t) = \sum_{i=1}^N \phi_i(\mathbf{x}, t) \nabla c_i(\mathbf{x}, t) + \nabla \phi_i(\mathbf{x}, t) \sum_{i=1}^N c_i(\mathbf{x}, t). \quad (10)$$

Similarly, the Allen-Cahn equation is given as

$$\dot{\phi}_i = -L_i(c, \phi_i) \nabla \left(\frac{\delta F}{\delta \phi_i} \right), \quad (11)$$

where $L_i(c, \phi_i)$ is the relaxation coefficient and $\frac{\delta F}{\delta \phi_i}$ is the variational derivative of the free energy function with respect to the phase-field variable. As pointed out by Steinbach et al. [23], this equation fails to define the relaxation coefficient L_i for triple or more junctions of grains. To overcome this, Steinbach et al. [23], introduced a step function $s_i(\mathbf{x}, t)$ such that

$$s_i(\mathbf{x}, t) = \begin{cases} 1 & \text{for } \phi_i > 0, \\ 0 & \text{otherwise} \end{cases} \quad (12)$$

so that the number of coexisting phases $n(\mathbf{x}, t)$ can be defined as

$$n(\mathbf{x}, t) = \sum_{i=1}^N s_i(\mathbf{x}, t). \quad (13)$$

Furthermore, by defining an interface field ψ_{ij} as $\psi_{ij} := \phi_i - \phi_j$ only at the interface of i -th and j -th phase, where $s_i \neq 0$ and $s_j \neq 0$, the constraint in (1) can be rewritten as

$$\phi_i = \frac{1}{n} \left[\sum_{j=1, j \neq i}^N s_i s_j \psi_{ij} + 1 \right], \quad (14)$$

resulting in the time derivative of the phase-field variables to be

$$\dot{\phi}_i = \frac{1}{n} \sum_{j=1, j \neq i}^N s_i s_j \frac{\partial \psi_{ij}}{\partial t} = \frac{1}{n} \sum_{j=1, j \neq i}^N s_i s_j \left[\frac{\partial \phi_i}{\partial t} - \frac{\partial \phi_j}{\partial t} \right]. \quad (15)$$

Note that the evolution of the phase-field variables take place only at the interface unlike the evolution of the composition-field variables, which only occur in the bulk of the system. Analogous, using the relaxation ansatz from Steinbach et al. [23, 57]

$$\frac{\delta \phi_i}{\delta t} - \frac{\delta \phi_j}{\delta t} = -2M_{ij} \left[\frac{\delta F}{\delta \phi_i} - \frac{\delta F}{\delta \phi_j} \right], \quad (16)$$

we can finally write (11) as

$$\dot{\phi}_i = -\frac{2}{n} \sum_{j=1, j \neq i}^N s_i s_j M_{ij} \left[\frac{\delta F}{\delta \phi_i} - \frac{\delta F}{\delta \phi_j} \right], \quad (17)$$

where M_{ij} is the phase-field mobility of the specific interface between two phases (or grains). The variational derivative of the free energy function with respect to the phase-field variables is calculated as

$$\begin{aligned} \frac{\delta F}{\delta \phi_i} &= \left[f_i(c_i) + \sum_{j=1}^N \phi_j f_j^c(c_j) \frac{\partial c_j}{\partial \phi_i} \right] + \sum_{j=1, j \neq i}^N \left[\frac{\epsilon_{ij}^2}{2} \nabla^2 \phi_j + \omega_{ij} \phi_j \right] - \lambda_\phi, \\ &= \left[f_i(c_i) + f^c \sum_{j=1}^N \phi_j \frac{\partial c_j}{\partial \phi_i} \right] + \sum_{j=1, j \neq i}^N \left[\frac{\epsilon_{ij}^2}{2} \nabla^2 \phi_j + \omega_{ij} \phi_j \right] - \lambda_\phi. \end{aligned} \quad (18)$$

Considering that the differentiation of (2) with respect to ϕ_i leads to $c_i + \sum_{j=1}^N \phi_j \frac{\partial c_j}{\partial \phi_i} = 0$, the variational derivative can be simplified to

$$\frac{\delta F}{\delta \phi_i} = [f_i(c_i) - c_i f^c] + \sum_{j=1, j \neq i}^N \left[\frac{\epsilon_{ij}^2}{2} \nabla^2 \phi_j + \omega_{ij} \phi_j \right] - \lambda_\phi. \quad (19)$$

Consequently, the Allen-Cahn equation becomes

$$\begin{aligned} \dot{\phi}_i = -\frac{2}{n} \sum_{j=1, j \neq i}^N s_i s_j M_{ij} \left[\frac{\epsilon_{ij}^2}{2} [\nabla^2 \phi_j - \nabla^2 \phi_i] + \omega_{ij} [\phi_j - \phi_i] + \sum_{k=1, k \neq i, j}^N s_k \left[\left[\frac{\epsilon_{ik}^2}{2} - \frac{\epsilon_{jk}^2}{2} \right] \nabla^2 \phi_k \right. \right. \\ \left. \left. + [\omega_{ik} - \omega_{jk}] \phi_k \right] + [[f_i - c_i f^c] - [f_j - c_j f^c]] \right]. \end{aligned} \quad (20)$$

2.2. Parameters of the multiphase-field model

The parameters required to implement the multiphase-field framework are chemical-free energy density of component i , f_i (and subsequently, the derivative of free energy density of component i with respect to the chemical composition c_i , f^c), gradient energy coefficient, ϵ_{ij} , energy barrier, ω_{ij} , mobility between the interface i and j , M_{ij} , and interdiffusion coefficient, D .

Considering the binary phase diagram of an Al-Mg system [58, 2], depending upon the composition range of the alloys, at temperatures under 450°C , the formation of Al_3Mg_2 and $\text{Al}_{12}\text{Mg}_{17}$ is expected. Furthermore, Al_3Mg_2 and $\text{Al}_{12}\text{Mg}_{17}$ is expected to form in the temperature range of interest for solid-state joining, see e.g. [19, 59, 60, 5]. To obtain the chemical-free energy density f_i consistent with the phase equilibrium diagram to get quantitative results, the CALPHAD method is used in the thermodynamic assessment of the Al-Mg system [61, 62, 63, 64]. To this end, assuming a constant molar volume fraction V_m for simplicity, the chemical-free energy density of various components of the Al-Mg system is extracted [61, 62, 63, 64] as follows:

$$\begin{aligned} f_{\text{Al}}^{\text{FCC}} V_m : \quad & c_{\text{Al}} f_{\text{Al}}^{\text{FCC}} + c_{\text{Mg}} f_{\text{Mg}}^{\text{FCC}} + RT [c_{\text{Al}} \ln(c_{\text{Al}}) + c_{\text{Mg}} \ln(c_{\text{Mg}})] + \\ & c_{\text{Al}} c_{\text{Mg}} [f_{0,\text{Al}} + f_{1,\text{Al}} [c_{\text{Al}} - c_{\text{Mg}}]], \end{aligned} \quad (21)$$

$$f_{\beta} V_m : \quad 1 \times 10^5 (c_{\text{Mg}} - 0.389)^2 + 0.6 f_{\text{Al}}^{\text{FCC}} + 0.4 f_{\text{Mg}}^{\text{HCP}} + \Delta f_{\beta}^f, \quad (22)$$

$$\begin{aligned} f_{\text{Mg}}^{\text{HCP}} V_m : \quad & c_{\text{Mg}} f_{\text{Mg}}^{\text{HCP}} + c_{\text{Al}} f_{\text{Al}}^{\text{HCP}} + RT [c_{\text{Mg}} \ln(c_{\text{Mg}}) + c_{\text{Al}} \ln(c_{\text{Al}})] + \\ & c_{\text{Mg}} c_{\text{Al}} [f_{0,\text{Mg}} + f_{1,\text{Mg}} [c_{\text{Mg}} - c_{\text{Al}}]]. \end{aligned} \quad (23)$$

where c_X denotes the composition of an element X, f_X^Y is the molar Gibbs energy of the pure element X with Y (either FCC or HCP) structure taken from Dinsdale [65]. The first two terms in (21) and (23) refer to the Gibbs energies of the mechanical mixture of the two components while the last two terms represent the excess molar Gibbs energy contribution showing the interaction energy based on the composition dependency given by Redlich-Kister polynomial, between various elements [64]. The intermetallic compounds Al_3Mg_2 is symbolically represented as β , so Δf_{β}^f are the Gibbs energy terms of formation per mole of atoms of Al_3Mg_2 . R is the ideal gas constant and T is the operating temperature. $f_{Y,X}$ are the Y-th binary interaction parameters, i.e. solution parameters for pure X element. Since the Al_3Mg_2 intermetallic phase is

Table 1. Analytical description of Al-Mg system [65, 61, 64] showing various Gibbs energy terms used in the current model as a function of temperature in Kelvin.

Parameter	Symbol	Analytical expression
Gibbs energy of the pure Al with FCC structure	$f_{\text{Al}}^{\text{FCC}}$	$-7976.15 + 137.093038 T$ $-24.3671976 T \ln(T)$ $-1.884662 \times 10^{-3} T^2$ $-0.877664 \times 10^{-6} T^3 + 74092 T^{-1}$
Gibbs energy of the pure Al with HCP structure	$f_{\text{Al}}^{\text{HCP}}$	$-2495.15 + 135.293038 T$ $-24.3671976 T \ln(T)$ $-1.884662 \times 10^{-3} T^2$ $-0.877664 \times 10^{-6} T^3 + 74092 T^{-1}$
Gibbs energy of the pure Mg with FCC structure	$f_{\text{Mg}}^{\text{FCC}}$	$-5767.34 + 142.775547 T$ $-26.1849782 T \ln(T)$ $+0.4858 \times 10^{-3} T^2$ $-1.393669 \times 10^{-6} T^3 + 78950 T^{-1}$
Gibbs energy of the pure Mg with HCP structure	$f_{\text{Mg}}^{\text{HCP}}$	$-8367.34 + 143.675547 T$ $-26.1849782 T \ln(T)$ $+0.4858 \times 10^{-3} T^2$ $-1.393669 \times 10^{-6} T^3 + 78950 T^{-1}$
Interaction/solution parameter for Al	$f_{0,\text{Al}}$	$+1593 + 2.149 T$
Interaction/solution parameter for Al	$f_{1,\text{Al}}$	$+1014 - 0.660 T$
Interaction/solution parameter for Al	$f_{2,\text{Al}}$	-673
Interaction/solution parameter for Mg	$f_{0,\text{Mg}}$	$+4336 - 2.863 T$
Interaction/solution parameter for Mg	$f_{1,\text{Mg}}$	$-449 - 0.135 T$
Interaction/solution parameter for Mg	$f_{2,\text{Mg}}$	-1963
Gibbs energy of formation per mole of atoms of Al_3Mg_2	Δf_{β}^f	$-1451 - 1.907 T$

described as a stoichiometric compound in the literature [61, 62, 63, 64], it would lead to a single point in the Gibbs energy framework, hence we assumed f_{β} to be a parabolic function of composition [66]. The expression for the parabolic function is set to ensure the solubility of the β -phase in aluminum. Since the computation of the Gibbs free energy of the $\text{Al}_{12}\text{Mg}_{17}$ phase is non-trivial because of the calculation of site fractions of Al/Mg in various sublattices [64], PanMg2017 database in PANDAT software is used to obtain it. Analogous to Al_3Mg_2 , the intermetallic compounds $\text{Al}_{12}\text{Mg}_{17}$ is denoted by γ . Table 1 gives the analytical description for the relevant Gibbs energy terms as a function of temperature. Using (21)–(23), one can easily compute f_i and f^c required for solving (20), as well as the equilibrium concentrations via so-called equilibrium conditions [67, 55], given by

$$f_i^c(e c_i) = f_j^c(e c_j) = \frac{f_j(e c_j) - f_i(e c_i)}{e c_j - e c_i}, \quad (24)$$

where ${}^e c_i$ is the equilibrium concentration of the i -th phase.

Suhuddin et al. [68] reported a typical thermal cycle during FSSW to be in the range of 370°C–450°C, while Panteli et al. [5] measured temperatures during ultrasonic welding in the range of 400°C–430°C. Hence, we compute Gibbs free energy of all four phases with respect to Mg concentration at 400°C as shown in Figure 1. The equilibrium phase compositions can thus be extracted and are summarized in Table 2.

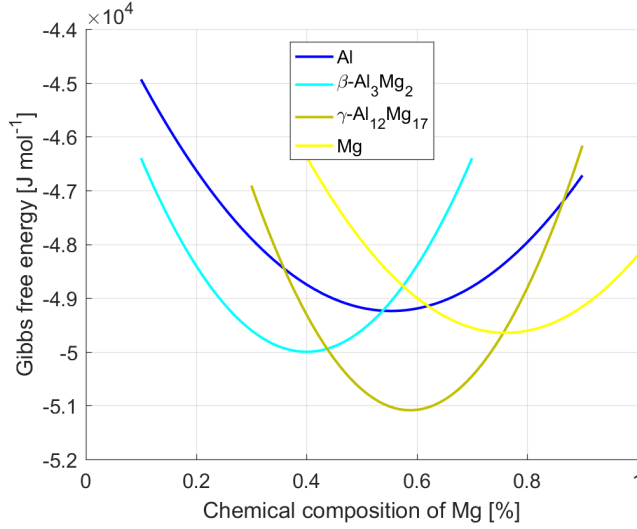


Figure 1. Gibbs free energy of various elements i.e. Al, Al_3Mg_2 , $\text{Al}_{12}\text{Mg}_{17}$ and Mg with respect to the concentration of Mg. This is computed by using (21)–(23), and Tables 1 and 3. Since Al_3Mg_2 is a stoichiometric phase, it is assumed to be a parabola.

Table 2. Equilibrium phase compositions (in mole fraction) with respect to the composition of Mg at $T = 400^\circ\text{C}$.

Phases	Equilibrium phase composition
${}^e c_{\text{Al}}$	0.14
${}^e c_{\beta}$	0.39
${}^e c_{\gamma}$	0.59
${}^e c_{\text{Mg}}$	0.90

The gradient energy coefficient ϵ_{ij} and the energy barrier ω_{ij} are dependent on the interface energy σ_{ij} and interface width ξ_{ij} as [69]

$$\epsilon_{ij} = \frac{4\sqrt{\sigma_{ij}\xi_{ij}}}{\pi}, \quad (25)$$

$$\omega_{ij} = \frac{2\sigma_{ij}}{\xi_{ij}}. \quad (26)$$

The atomic mobility M_{ij} is defined as [69]:

$$M_{ij} = \frac{\bar{D}_{ij}\sigma_{ij}\sqrt{2\omega_{ij}}}{[{}^e c_i - {}^e c_j]^2 f^{c,c} \epsilon_{ij}^3 K} \quad \text{with} \quad K = \int_0^1 \frac{\sqrt{\phi[1-\phi]}}{\bar{k} + [1-\bar{k}]\phi} d\phi, \quad (27)$$

where $\bar{k} = \frac{e c_i}{e c_j}$, $\bar{D}_{ij} = \max(D_i, D_j)$ and $e c_i$ is the equilibrium concentration of i -th phase obtained from Figure 1 (and Table 2). As suggested by Kim et al. [69], M_{ij} is considered to be uniform throughout each phase interface as $M = \max(M_{ij})$. It is well known that the interfacial energies σ_{ij} and mobilities M_{ij} are difficult to determine experimentally or computationally [70], hence, we assume the values of σ_{ij} in this work and consider these as simulation parameters.

3. Simulation setup

3.1. Initial microstructure model

To illustrate the capability of the multiphase-field approach, a two-dimensional model is constructed on MATLAB to simulate the temperature-driven diffusion involving FSSW of Al and Mg. To this end, an initial microstructure with various components is assumed, as shown in Figure 2, where the bulk Al and Mg are to be joined and intermetallic compounds Al_3Mg_2 and $\text{Al}_{12}\text{Mg}_{17}$ are assumed to be formed at the interface. As an idealistic structure, we set the initial thickness of Al_3Mg_2 layer to $0.5\mu\text{m}$ and grain size between $0.1 - 0.6\mu\text{m}$, while for $\text{Al}_{12}\text{Mg}_{17}$, the layer thickness is set to $0.6\mu\text{m}$ with a grain size of $0.1 - 0.7\mu\text{m}$. Note that the initial $\text{Al}_{12}\text{Mg}_{17}$ layer thickness is set larger than for the Al_3Mg_2 layer, since during diffusion bonding $\text{Al}_{12}\text{Mg}_{17}$ tends to form first before the formation of Al_3Mg_2 [5, 60]. Interfaces Al/ Al_3Mg_2 and $\text{Al}_{12}\text{Mg}_{17}$ /Mg, as well as the grain boundaries are explicitly defined in the initial microstructure. The common boundary of the two intermetallic compounds is assumed to have no mobility and interface energy, to ensure that Al_3Mg_2 grow predominantly in the Al side while $\text{Al}_{12}\text{Mg}_{17}$ on the Mg side as noticed experimentally by Panteli et al. [5].

The initial microstructure is discretized by the finite difference method of uniform lattice space Δx . To tackle the problem at hand, 100 phase-field variables ϕ_i are selected, i.e. $i = 1 - 100$ where $\phi_1 = 1$ for Al bulk phase, $\phi_i = 1$ with $2 \leq i < 51$ for the Al_3Mg_2 , $\phi_i = 1$ with $52 \leq i < 100$ for the $\text{Al}_{12}\text{Mg}_{17}$ and $\phi_{100} = 1$ for Mg bulk phase. Phase-field variables for the intermetallic compound layer ($\phi_i = 1$ for $2 \leq i \leq 99$) represent randomly generated grains. Distinct diffusion coefficients are defined for eight regions: D_j , where $j = \text{Al}$, Al/ β interface, β grains, β grain boundaries, γ grains, γ grain boundaries, γ /Mg interface, Mg. The designation of the diffusion coefficient $D(\phi_i)$

|| Different number of phase-field variables are reported in literature, e.g. [66, 70], based on the applications. Note that the number of phase-field variable directly impacts the computational time.

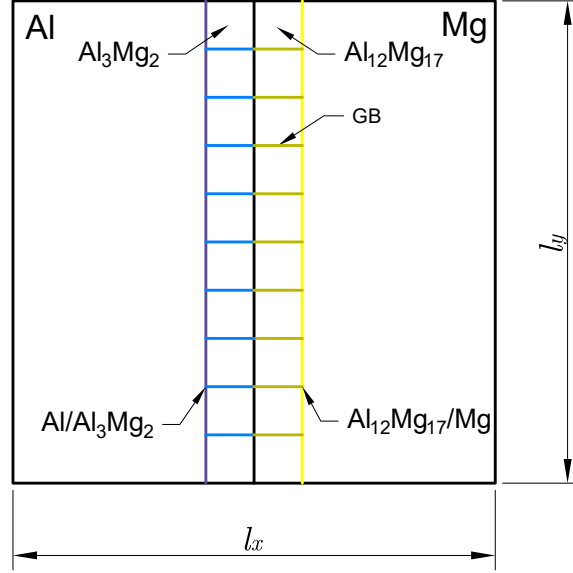


Figure 2. Representation of the initial microstructure, consisting of Al, Mg, Al_3Mg_2 and $\text{Al}_{12}\text{Mg}_{17}$ components. The Al/ Al_3Mg_2 boundary (purple), $\text{Al}_{12}\text{Mg}_{17}$ /Mg boundary (yellow), Al_3Mg_2 grain boundaries (blue), $\text{Al}_{12}\text{Mg}_{17}$ grain boundaries (olive), and grain boundaries between two intermetallic compounds (black) are defined in the initial microstructure. Diffusion rates are defined for the bulk Al, Mg, Al_3Mg_2 and $\text{Al}_{12}\text{Mg}_{17}$ along with the boundaries between Al/ Al_3Mg_2 , $\text{Al}_{12}\text{Mg}_{17}$ /Mg and intermetallic compounds grain boundaries (GB). See Table 3 for material properties.

is then as follows [49]:

$$\begin{aligned}
 & \text{if } \phi_{\text{Al}} \geq 0.8 \Rightarrow D = D_{\text{Al}} \\
 & \text{if } \phi_{\text{Mg}} \geq 0.8 \Rightarrow D = D_{\text{Mg}} \\
 & \text{if } 0.8 > \phi_{\text{Al}} > 0.2 \Rightarrow D = D_{\text{Al}/\beta} \\
 & \text{if } 0.8 > \phi_{\text{Mg}} > 0.2 \Rightarrow D = D_{\gamma/\text{Mg}} \\
 & \text{if } \phi_{\beta} \geq 0.8 \Rightarrow D = D_{\beta} \\
 & \text{if } \phi_{\gamma} \geq 0.8 \Rightarrow D = D_{\gamma} \\
 & \text{else } \Rightarrow D = D_{\beta/\gamma\text{GB}}
 \end{aligned} \tag{28}$$

The boundary condition is set to be of Neumann type on all sides. A summary of the material parameters used in the current multiphase-field model is given in Table 3.

Table 3. Material parameters used in the current multiphase-field model. Static diffusion rates are assumed from Brennan et al. [71] for simplicity. Gibbs energy and excess molar are computed as per Table 1 at $T = 400^\circ\text{C}$. The mobility and diffusivity of the intermetallic compound grain boundaries is usually taken higher than that of the bulk regions e.g. [66, 69], a similar approach is adopted in this work. Interface energies are set as simulation parameters.

Parameter	Symbol	Magnitude	Unit
Working temperature	T	$400 + 273.15$	K
Lattice spacing	Δx	1×10^{-7}	m
Grid size	$l_x \times l_y$	$400\Delta x \times 200\Delta x$	m \times m
Interface width	ξ_{ij}	$4\Delta x$	m
Ideal gas constant	R	8.314	J mol $^{-1}$ K $^{-1}$
Boltzmann constant	k_B	$1.38064852 \times 10^{-23}$	J K $^{-1}$
Molar Volume	V_m	0.55×10^{-5}	m 3 mol $^{-1}$
Diffusion rate of Al [71, 72]	D_{Al}	1.9×10^{-14}	m 2 s $^{-1}$
Diffusion rate of Mg [71, 72]	D_{Mg}	4.9×10^{-15}	m 2 s $^{-1}$
Diffusion rate of Al $_3$ Mg $_2$ [71, 72]	D_β	2.4×10^{-12}	m 2 s $^{-1}$
Diffusion rate of Al $_{12}$ Mg $_{17}$ [71, 72]	D_γ	1.3×10^{-13}	m 2 s $^{-1}$
Diffusion rate between Al and Al $_3$ Mg $_2$	$D_{\text{Al}/\beta}$	$D_{\text{Al}} \times 10^2$	m 2 s $^{-1}$
Diffusion rate between Al $_{12}$ Mg $_{17}$ and Mg	$D_{\gamma/\text{Mg}}$	$D_{\text{Mg}} \times 10^2$	m 2 s $^{-1}$
Diffusion rate between Al $_3$ Mg $_2$ grains	$D_{\text{GB},\beta}$	$D_{\text{Al}} \times 10^2$	m 2 s $^{-1}$
Diffusion rate between Al $_{12}$ Mg $_{17}$ grains	$D_{\text{GB},\gamma}$	$D_{\text{Mg}} \times 10^2$	m 2 s $^{-1}$
Mobility of the boundary Al/Al $_3$ Mg $_2$	$M_{\text{Al}/\beta}$	1.5874×10^{-8}	m 2 s $^{-1}$
Mobility of the boundary Al $_{12}$ Mg $_{17}$ /Mg	$M_{\gamma/\text{Mg}}$	5.4518×10^{-9}	m 2 s $^{-1}$
Mobility of grain boundaries	M_{GB}	$\max(M_{\text{Al}/\beta}, M_{\gamma/\text{Mg}})$	m 2 s $^{-1}$
Interface energy of the boundary Al/Al $_3$ Mg $_2$	$\sigma_{\text{Al}/\beta}$	15	J m $^{-2}$
Interface energy of the boundary Al $_{12}$ Mg $_{17}$ /Mg	$\sigma_{\gamma/\text{Mg}}$	15	J m $^{-2}$
Interface energy of the grain boundaries	σ_{GB}	$2\sigma_{\gamma/\text{Mg}} = 2\sigma_{\text{Al}/\beta}$	J m $^{-2}$

3.2. Numerical implementation

Among many methods available to solve (9) and (20), as reviewed in Bellemans et al. [73], in the present work, we use an explicit finite-difference approach for two-dimensional square lattices with uniform lattice spacing Δx . As per Huh et al. [49], two grids are defined: the first for phase fields and compositions, and the second for diffusion flux where nodal points are located at the midpoint of the first grid. The fluxes are computed at the nodal point of the second grid by solving (5). To do this, $D(\phi_i)$ at the nodal point of the second grid is calculated by determining ϕ_i where $i = 1, \dots, N$,

using Lagrange interpolation on the four neighboring nodal points of the first grid. The discrete time step in such cases is typically set as [24]

$$\Delta t < \frac{1}{2} \frac{[\Delta x]^2}{D_{\max}}, \quad (29)$$

where D_{\max} is the largest of all diffusivities in the present system. The partial differential equations (4) and (11) contain both derivatives in space and time, resulting in a need for discretization in both domains. The time evolution of a variable Ω , i.e. either the phase-field variable ϕ or composition-field variable c , is given by

$$\Omega(i, j, t + \Delta t) = \Omega(i, j, t) + \frac{\partial \Omega}{\partial t}(i, j, t) \Delta t. \quad (30)$$

The Laplacian present in (20) can be evaluated for the two-dimensional case as

$$\nabla^2 \phi_{i,j} = \frac{1}{6\Delta x^2} [\phi_{i-1,j-1} + \phi_{i+1,j+1} + \phi_{i+1,j-1} + \phi_{i-1,j+1} + 4\phi_{i-1,j} + 4\phi_{i+1,j} + 4\phi_{i,j-1} + 4\phi_{i,j+1} - 20\phi_{i,j}]. \quad (31)$$

Algorithm 1 shows the update scheme of the phase- and the composition-field variables.

Algorithm 1 Phase-field and composition-field variables update

- 1: Input arguments: Δt , Δx , R , T , M_{ij} , D , σ_{ij} , $\phi_{i,t}$ where $i = 1, \dots, N$, $c_{i,t}$ where $i = 1, \dots, N$, V_m , k_B .
 - 2: Assign M_{ij} , D , σ_{ij} , ϕ_i , and c_i given in Table 3 to different components in the system, based on the initial microstructure shown in Figure 2.
 - 3: Compute f_i from (21)–(23) and f^c their derivatives with respect to the composition variable.
 - 4: Compute ϵ_{ij} and ω_{ij} using (25) and (26), respectively.
 - 5: Compute the evolution of composition-field variables \dot{c}_i using (9).
 - 6: Discretize composition-field variables c_i to get $c_{i,t+\Delta t}$ using (30).
 - 7: Compute the evolution of phase-field variables $\dot{\phi}_i$ using (20).
 - 8: Discretize phase-field variable ϕ_i to get $\phi_{i,t+\Delta t}$ using (30). Solve the Laplacian using (31).
 - 9: Return $\phi_{i,t+\Delta t}$ and $c_{i,t+\Delta t}$.
-

4. Results

The purpose of the simulation is to investigate the intermetallic compounds, namely, Al_3Mg_2 and $\text{Al}_{12}\text{Mg}_{17}$ in an Al-Mg system and their dependence on diffusivities and interface energy of the grain boundary. Keeping in view the temperature range of interest for FSSW of Al and Mg [68], all parameters and consequently the simulation

is carried out at 400°C. Furthermore, during the FSSW experiments of Al and Mg alloys by Suhuddin et al. [68], the typical dwell time was set to 2s. Assuming that the intermetallic layer mainly grows within this time frame, comparisons of the layer thickness and grains morphology between experiment and simulation would be made at a simulation time of 2s. To this end, we present the results on the morphology and evolution of intermetallic compounds at various time intervals, along with the impact of grain boundary diffusion as well as interface energy on it.

4.1. Evolution of the morphology and thickness of the intermetallic compounds

With the material parameters set in Table 3, Figure 3 exhibits the evolution of the intermetallic compound at various times t_i during the simulation. The overall thickness

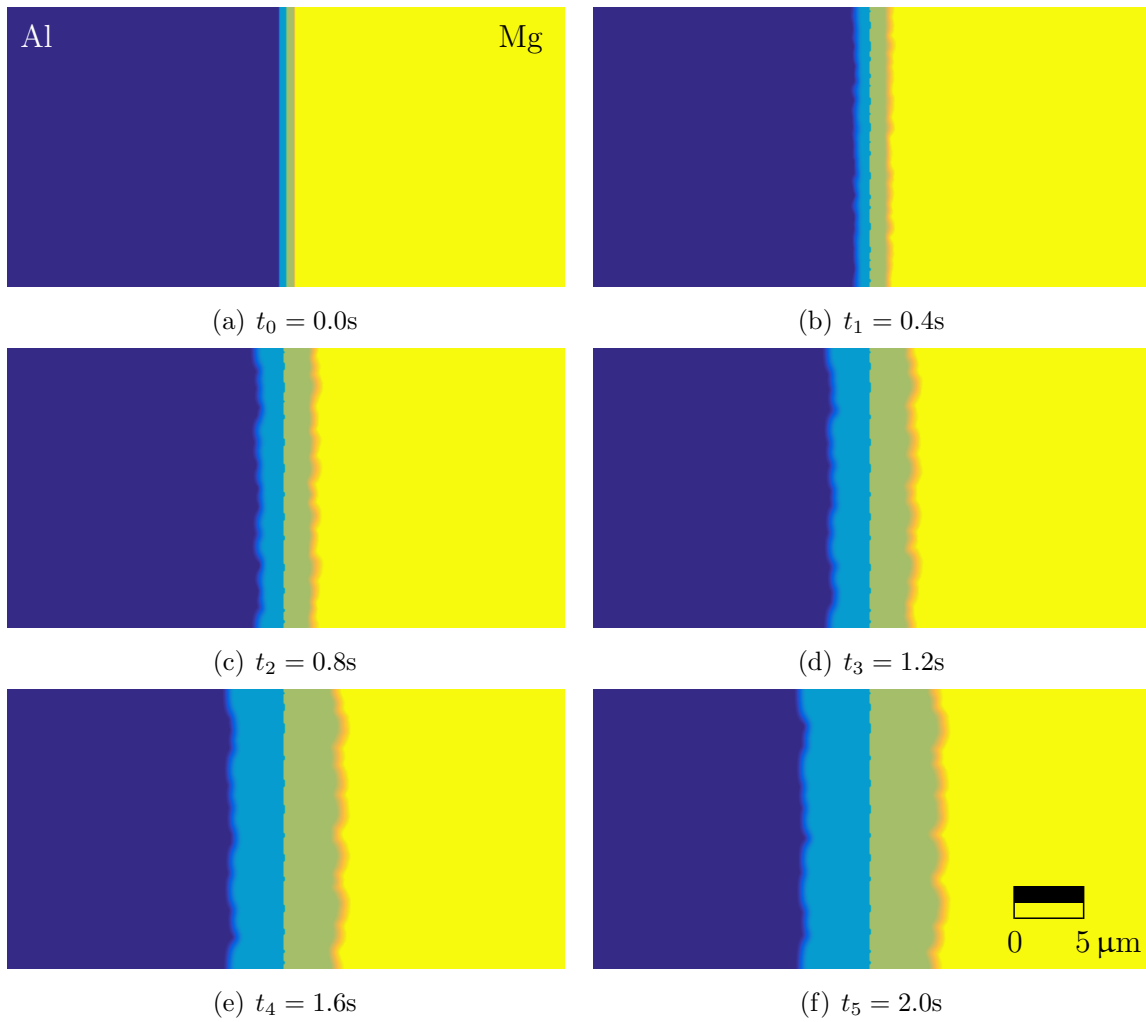


Figure 3. Evolution of intermetallic compounds at different stages of the simulation based on the material properties set in Table 3. The overall thickness of Al_3Mg_2 (cyan) and $\text{Al}_{12}\text{Mg}_{17}$ (olive) are determined to be $4\mu\text{m}$ and $5\mu\text{m}$, respectively, at the time $t_5 = 2.0\text{s}$.

of the intermetallic compound is found to be $9\mu\text{m}$, where the thickness of Al_3Mg_2 and

$\text{Al}_{12}\text{Mg}_{17}$ is $4\mu\text{m}$ and $5\mu\text{m}$, respectively, after 2s simulation time. Jafarian et al. [59] observed the transition intermetallic on the Mg side to be always greater than the intermetallic layer on the Al side. Suhuddin et al. [19] measured the thickness of the intermetallic compounds to be in the range of $7 - 20\mu\text{m}$. However, they argued that the higher thickness of intermetallic compound was observed at the location where a higher degree of material flow took place. Due to severe plastic deformation as a result of material flow, an enhanced diffusion rate is expected [68]. The overall obtained thickness of $9\mu\text{m}$ falls on the lower end of the range since only the temperature-driven evolution of intermetallic is considered. To exhibit the morphology evolution, Figure 4 shows the evolution of phase-field variables. It can be seen that the evolution of

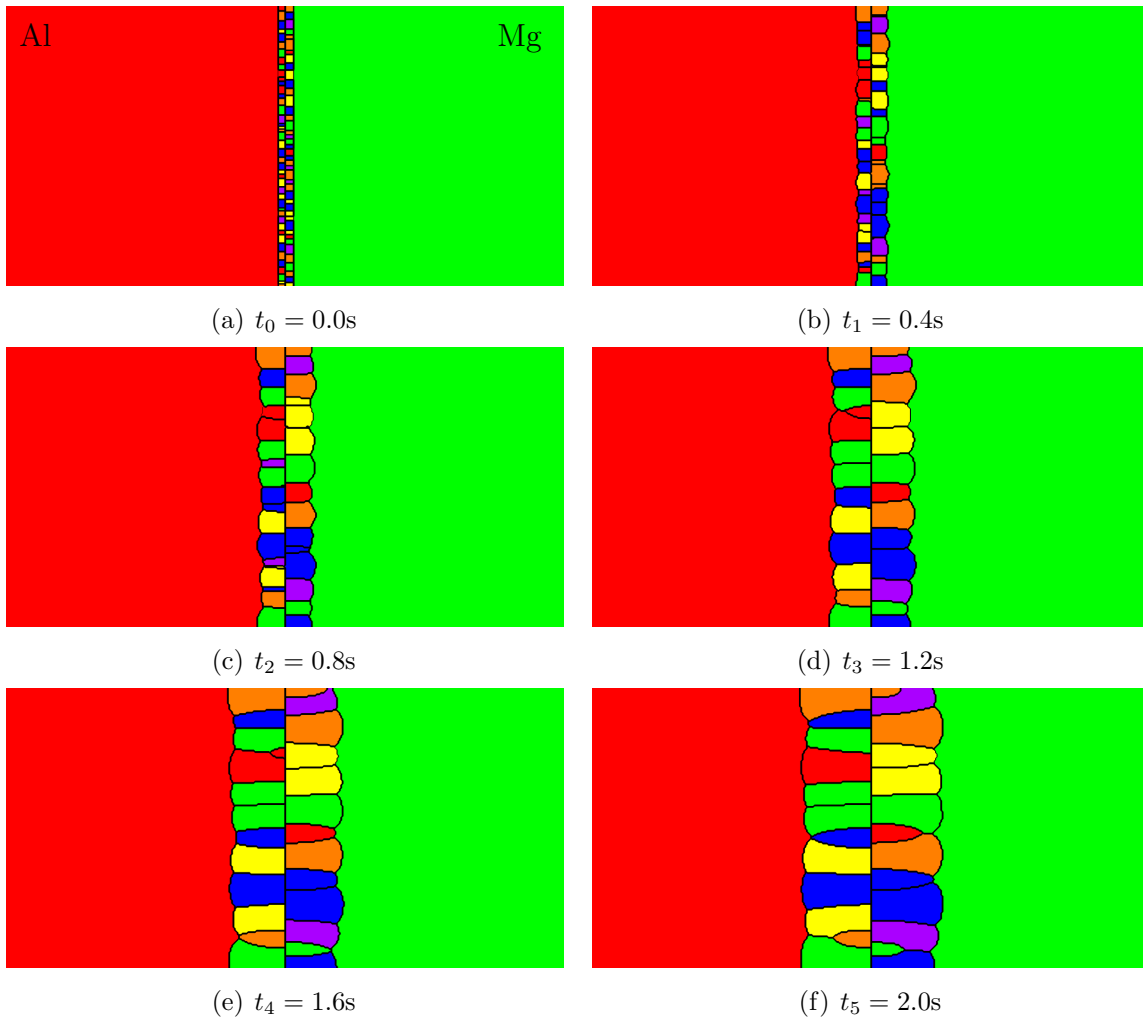


Figure 4. Evolution of phase-fields at different stages of the simulation based on the material properties set in Table 3. The red color denotes Al while the green color denotes Mg. Multicolor regions at the interface show various grains of the intermetallic compound.

the intermetallic compounds Al_3Mg_2 and $\text{Al}_{12}\text{Mg}_{17}$ lead to a columnar structure. This was also experimentally observed by Panteli et al. [5] during the ultrasonic welding of an Al/Mg system, indicating a qualitative agreement of the simulation results to

experiments. Next, the evolution of the solute composition-field variable is illustrated in Figure 5. It can be observed that the simulation shows the principal mechanism

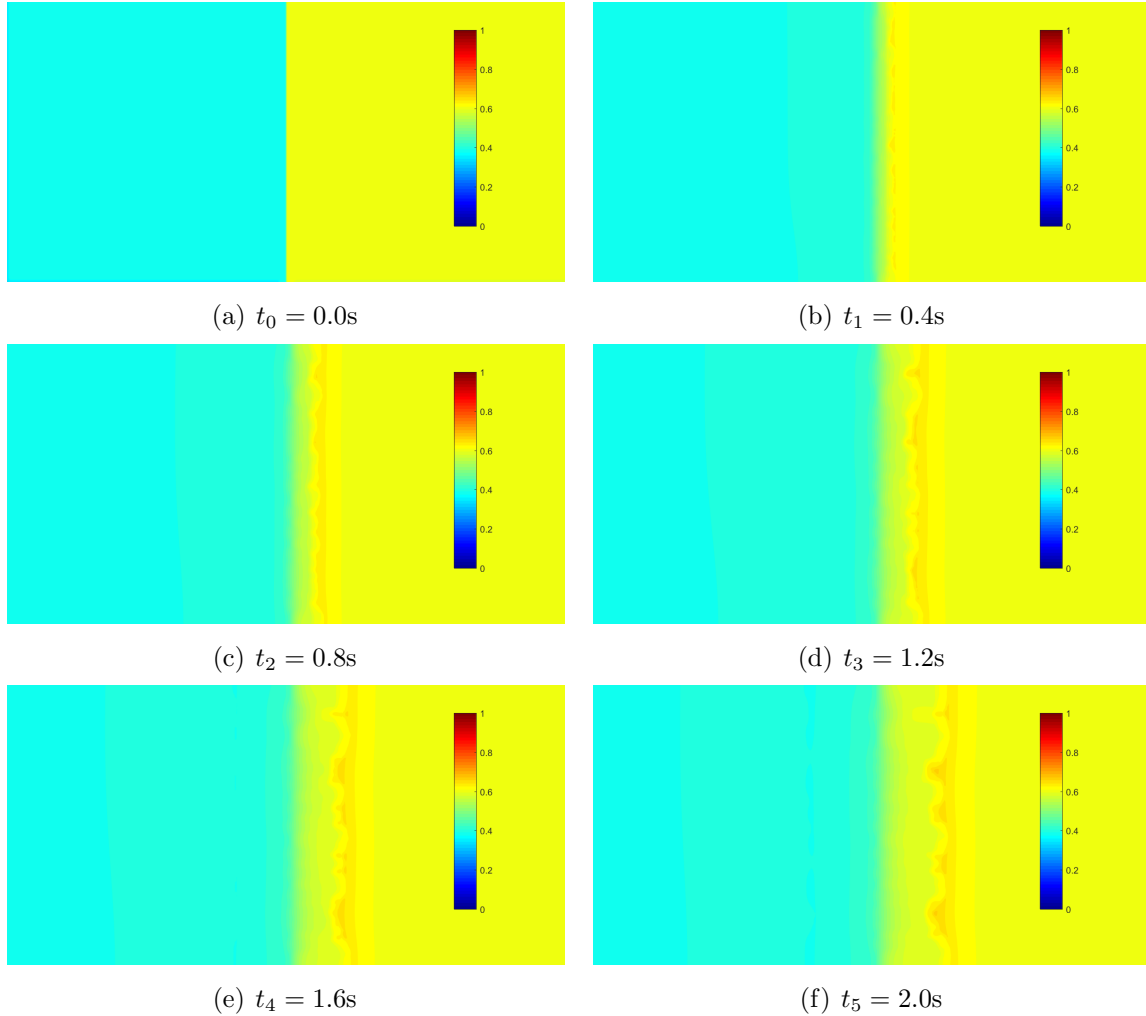


Figure 5. Composition-field evolution of intermetallic compound grains at different stages of the simulation based on the material properties set in Table 3.

known as the Gibbs-Thomson effect (or curvature effect). The curved surface with higher composition creating a gradient with planar surfaces, driving the microstructure evolution.

4.2. Effect of grain boundary diffusion on the morphology and kinetics of the intermetallic compounds

Two mechanisms control the microstructural evolution of the intermetallic compound: the grain boundary diffusion, and the interface curvature effect driving the diffusion, i.e. the Gibbs-Thomson effect [49]. The grain boundary diffusion is responsible for the initial mass fluxes required for intermetallic compound growth, i.e. Mg and Al fluxes with Al and Mg substrate, respectively, towards the grain boundary junction.

Interface curvature effect related diffusion is the agent for the distribution of fluxes from the grain boundary to Al/Al₃Mg₂ and Al₁₂Mg₁₇/Mg interfaces. The effect of the two mechanisms dictates the groove shapes at the grain boundary junctions [49]. Although the grains are initially assumed to be square in shape, the grain growth results in rounded borders. Furthermore, the Al₃Mg₂ grains at the Al side are rounder compared to the Al₁₂Mg₁₇ grains at the Mg side. This is essentially due to the higher diffusion rate of Al/Al₃Mg₂ interface compared to Al₁₂Mg₁₇/Mg interface, i.e. $D_{Al/\beta} > D_{\gamma/Mg}$. To investigate the effect of grain boundary diffusion, a case where the diffusion coefficient of the grain boundary and intermetallic compounds is not enhanced, i.e. $D_{GB,\beta} = D_{\beta}$ and $D_{GB,\gamma} = D_{\gamma}$, is investigated and compared to the previous simulation, see Figures 6(a) and (b). The reduction of the diffusion coefficients results in the penetration of Al and Mg in the Al₃Mg₂ and Al₁₂Mg₁₇ phases, respectively, since the energy reduction of the system is mainly carried through grain boundary area reduction. Although the grain boundary is still the favorable diffusion path for the intermetallic layer growth due to the small diffusion distance along the grain boundary, the lower diffusivity slows down the growth rate of the intermetallic layer in comparison to the fast grain boundary as assumed in the previous simulation case. This also leads to less coarsening of the intermetallic compound grains due to the smaller tendency for competitive grain growth [49], as shown in Figure 6(b). Figure 6(d), which shows the combined effect of interface energy and grain boundary diffusion in terms of the obtained morphology, is a prime example of competitiveness between the two mechanisms. It can be observed that at higher interface energy, the effect of grain boundary energy is not pronounced with regards to the intermetallic compound kinetics. Figure 7 shows the Al₁₂Mg₁₇ intermetallic compound growth in terms of number of grids with, i.e. $D_{GB,\gamma} = D_{\gamma} \times 10^2$ (black), and without, i.e. $D_{GB,\gamma} = D_{\gamma}$ (blue), enhanced grain boundary diffusivity, while the energy of Al/Al₃Mg₂ and Al₁₂Mg₁₇/Mg interface is kept same in both cases, i.e. $\sigma_{Al/\beta} = \sigma_{\gamma/Mg} = 15 \text{ J m}^{-2}$. It can be seen that in the initial stages of the process, there is no growth of Al₁₂Mg₁₇ but broadening of interface and grain boundary. Furthermore, in both cases, the composition of the Mg decreases due to the curvature effect of Al₁₂Mg₁₇ boundaries, resulting in the dissolution of Al₁₂Mg₁₇ grains into Mg, which lead to a slight decrease of Al₁₂Mg₁₇ thickness. After a certain period, Al₁₂Mg₁₇ grain boundary grooves develop and the planar Al₁₂Mg₁₇ takes the rounded form. Finally, the enhanced grain boundary diffusion case results in a higher Al₁₂Mg₁₇ layer thickness.

4.3. Effect of interface energy on the morphology and kinetics of the intermetallic compounds

Intermetallic compound grain coarsening effect with respect to the the growth kinetics is investigated through varying the interface energy. To this end, the interface energy of the Al/Al₃Mg₂ and Al₁₂Mg₁₇/Mg interfaces is doubled, i.e. $\sigma_{Al/\beta} = \sigma_{\gamma/Mg} = 30 \text{ J m}^{-2}$, keeping the rest of the parameters same as mentioned in Table 3. In theory, this should incorporate higher tendency of competitive grain growth at the bulk material and

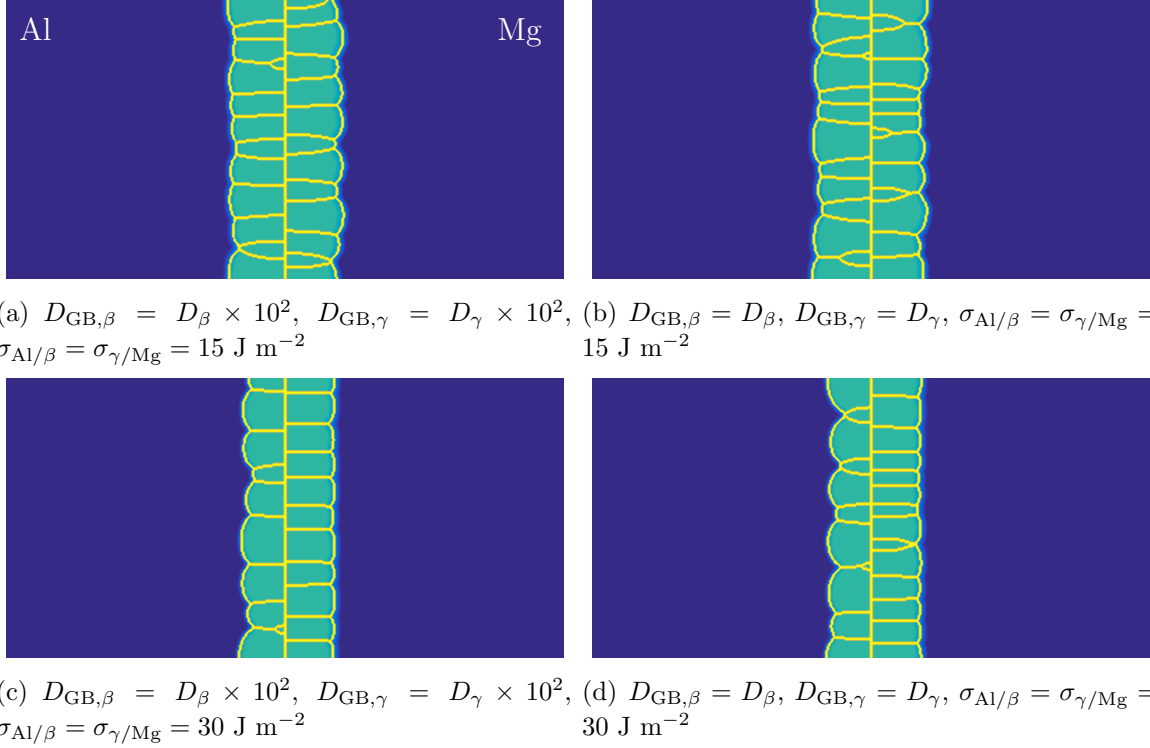


Figure 6. Intermetallic compound grain growth at time $t_4 = 1.6\text{s}$, showing various morphologies obtained by varying either diffusivities and/or interface energy. The blue color represents the bulk Al and Mg, the teal region shows the intermetallic compound with yellow lines as various grains. It can be observed that lower grain boundary diffusion leads to less grain coarsening, planar interfaces instead of rounded, and lower kinetics; whereas higher interface energy leads to more grain coarsening but lower kinetics.

intermetallic compound interface, resulting in the increase of the intermetallic compound grain coarsening rate, and thus, decrease in the intermetallic compound layer growth rate. This is indeed observed in Figure 6(c), which shows a comparison of Al_3Mg_2 and $\text{Al}_{12}\text{Mg}_{17}$ grain morphology at time $t_4 = 1.6\text{s}$ when $\sigma_{Al/\beta} = \sigma_{\gamma/Mg} = 30 \text{ J m}^{-2}$, showing more coarsening as compared to Figure 6(a) where lower interface energy is set.

Figure 7 shows the comparison of the growth of $\text{Al}_{12}\text{Mg}_{17}$ intermetallic compound when $\sigma_{Al/\beta} = \sigma_{\gamma/Mg} = 15 \text{ J m}^{-2}$ (black) and $\sigma_{Al/\beta} = \sigma_{\gamma/Mg} = 30 \text{ J m}^{-2}$ (green), keeping the grain boundary diffusion constant for both cases, i.e. $D_{GB,\gamma} = D_{\gamma} \times 10^2$. The increased $\sigma_{\gamma/Mg}$ value results in the higher competitive growth tendency, in comparison to lower $\sigma_{\gamma/Mg}$ value. This in turn speeds up the coarsening rate of the grains, thereby decreasing the $\text{Al}_{12}\text{Mg}_{17}$ growth rate, as can be seen in Figure 7.

5. Conclusion

A multiphase-field model for the intermetallic compounds Al_3Mg_2 and $\text{Al}_{12}\text{Mg}_{17}$ evolution during the solid-state joining of Al and Mg, assuming the joining process in this work as a purely temperature-driven diffusion process, is developed. The

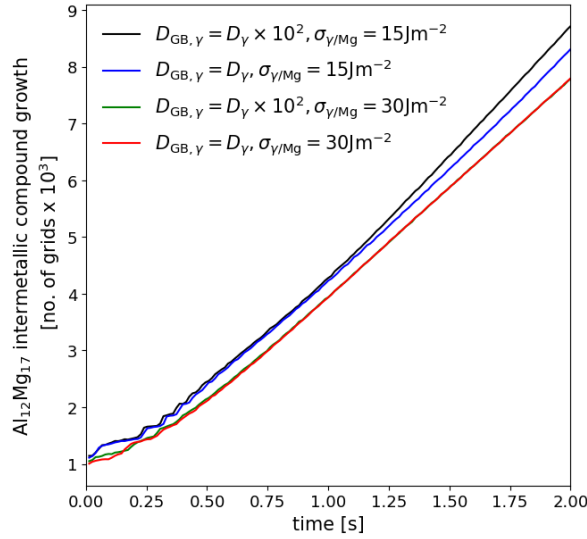


Figure 7. Variation in the growth kinetics of the intermetallic compound $\text{Al}_{12}\text{Mg}_{17}$ as a function of grain boundary diffusion and interface energy. Four cases are shown here: $D_{\text{GB},\beta} = D_{\beta} \times 10^2$, $D_{\text{GB},\gamma} = D_{\gamma} \times 10^2$, $\sigma_{\text{Al}/\beta} = \sigma_{\gamma/\text{Mg}} = 15 \text{ J m}^{-2}$ (black); $D_{\text{GB},\beta} = D_{\beta}$, $D_{\text{GB},\gamma} = D_{\gamma}$, $\sigma_{\text{Al}/\beta} = \sigma_{\gamma/\text{Mg}} = 15 \text{ J m}^{-2}$ (blue); $D_{\text{GB},\beta} = D_{\beta} \times 10^2$, $D_{\text{GB},\gamma} = D_{\gamma} \times 10^2$, $\sigma_{\text{Al}/\beta} = \sigma_{\gamma/\text{Mg}} = 30 \text{ J m}^{-2}$ (green); $D_{\text{GB},\beta} = D_{\beta}$, $D_{\text{GB},\gamma} = D_{\gamma}$, $\sigma_{\text{Al}/\beta} = \sigma_{\gamma/\text{Mg}} = 30 \text{ J m}^{-2}$ (red). It can be seen that higher grain boundary diffusion and lower interface energy leads to higher intermetallic compound growth. Furthermore, at higher interface energy the effect of grain boundary diffusion with respect to kinetics diminishes, i.e. varying both grain boundary diffusion and interface energy, the intermetallic compound growth is nearly identical (green and red curves).

framework of the multiphase-field model involves the calculation of the chemical-free energy function via the CALPHAD method whereas the kinetic parameters such as diffusion rates are obtained from the literature. The model is capable of modeling the intermetallic compound growth in a binary alloy system and shows to be able to predict the morphology as well as the thickness evolution of these intermetallic compounds qualitatively. The effect of the grain boundary diffusion and interface energy on the morphology and thickness of the intermetallic compound is investigated and the framework found to be capable of accounting for these two factors. Competitiveness between the fast GB diffusion to thicken the intermetallic layer and the diffusion driven by the Gibbs-Thomson effect to reduce the interface area dictates the morphology of the intermetallic compounds. Interface energy of the intermetallic compound and the bulk material drives the coarsening of the intermetallic compound. The simulation results give physically reasonable intermetallic compounds kinetics and are qualitatively comparable with published experimental results of intermetallic compound structures in solid-state processes in terms of layer thickness and shape. In the future, additional terms required to incorporate the effect of plastic deformation on the diffusion process will be investigated to analyze their effect on the intermetallic compound kinetics.

Acknowledgment

The authors would like to acknowledge Dr. Kuijing Song for her initial work on the development of the original code used in this study. Jan Herrring, Uceu Suhuddin, and George Diyoke are kindly acknowledged for constructive discussions.

References

- [1] Rios PR, Siciliano Jr F, Sandim HRZ, Plaut RL, Padilha AF. Nucleation and growth during recrystallization. *Materials Research*. 2005;8(3):225–238.
- [2] Liu L, Ren D, Liu F. A review of dissimilar welding techniques for magnesium alloys to aluminum alloys. *Materials*. 2014;7(5):3735–3757.
- [3] Lehmhus D, Busse M, Herrmann A, Kayvantash K. *Structural materials and processes in transportation*. John Wiley & Sons; 2013.
- [4] Yan J, Xu Z, Li Z, Li L, Yang S. Microstructure characteristics and performance of dissimilar welds between magnesium alloy and aluminum formed by friction stirring. *Scripta Materialia*. 2005;53(5):585–589.
- [5] Panteli A, Robson J, Brough I, Prangnell P. The effect of high strain rate deformation on intermetallic reaction during ultrasonic welding aluminium to magnesium. *Materials Science and Engineering: A*. 2012;556:31–42.
- [6] McLean A, Powell G, Brown I, Linton V. Friction stir welding of magnesium alloy AZ31B to aluminium alloy 5083. *Science and Technology of Welding and Joining*. 2003;8(6):462–464.
- [7] Plaine A, Gonzalez A, Suhuddin U, Dos Santos J, Alcântara N. The optimization of friction spot welding process parameters in AA6181-T4 and Ti6Al4V dissimilar joints. *Materials & Design*. 2015;83:36–41.
- [8] Schilling C, dos Santos J. Method and device for joining at least two adjoining work pieces by friction welding. Google Patents; 2004. US Patent 6,722,556.
- [9] Yang X, Fu T, Li W. Friction stir spot welding: a review on joint macro-and microstructure, property, and process modelling. *Advances in Materials Science and Engineering*. 2014;2014:11.
- [10] Rosendo T, Parra B, Tier M, Da Silva A, Dos Santos J, Strohaecker T, et al. Mechanical and microstructural investigation of friction spot welded AA6181-T4 aluminium alloy. *Materials & design*. 2011;32(3):1094–1100.
- [11] Mazzaferro JAE, Rosendo TdS, Mazzaferro CCP, Ramos FD, Tier MAD, Strohaecker TR, et al. Preliminary study on the mechanical behavior of friction spot welds. *Soldagem & Inspeção*. 2009;14(3):238–247.
- [12] Campanelli LC, Suhuddin UFH, Antonialli AÍ, Dos Santos JF, De Alcantara NG, Bolfarini C. Metallurgy and mechanical performance of AZ31 magnesium alloy friction spot welds. *Journal of Materials Processing Technology*. 2013;213(4):515–521.
- [13] Oliveira P, Amancio-Filho S, Dos Santos J, Hage Jr E. Preliminary study on the feasibility of friction spot welding in PMMA. *Materials Letters*. 2010;64(19):2098–2101.
- [14] Effertz P, Infante V, Quintino L, Suhuddin U, Hanke S, Dos Santos J. Fatigue life assessment of friction spot welded 7050-T76 aluminium alloy using Weibull distribution. *International journal of fatigue*. 2016;87:381–390.
- [15] Lee CY, Choi DH, Yeon YM, Jung SB. Dissimilar friction stir spot welding of low carbon steel and Al–Mg alloy by formation of IMCs. *Science and Technology of Welding and Joining*. 2009;14(3):216–220.
- [16] Gerlich A, Su P, North T. Peak temperatures and microstructures in aluminium and magnesium alloy friction stir spot welds. *Science and technology of welding and joining*. 2005;10(6):647–652.
- [17] Tozaki Y, Uematsu Y, Tokaji K. Effect of processing parameters on static strength of dissimilar friction stir spot welds between different aluminium alloys. *Fatigue & Fracture of Engineering Materials & Structures*. 2007;30(2):143–148.
- [18] Liyanage T, Kilbourne J, Gerlich A, North T. Joint formation in dissimilar Al alloy/steel and Mg alloy/steel friction stir spot welds. *Science and Technology of Welding and Joining*. 2009;14(6):500–508.
- [19] Suhuddin U, Fischer V, Kroeff F, Dos Santos J. Microstructure and mechanical properties of friction spot welds of dissimilar AA5754 Al and AZ31 Mg alloys. *Materials Science and Engineering: A*. 2014;590:384–389.

- [20] Zettler R, Da Silva AAM, Rodrigues S, Blanco A, dos Santos JF. Dissimilar Al to Mg alloy friction stir welds. *Advanced Engineering Materials*. 2006;8(5):415–421.
- [21] Khodir SA, Shibayanagi T. Dissimilar friction stir welded joints between 2024-T3 aluminum alloy and AZ31 magnesium alloy. *Materials transactions*. 2007;48(9):2501–2505.
- [22] Plaine A, Suhuddin U, Alcântara N, Dos Santos J. Microstructure and mechanical behavior of friction spot welded AA6181-T4/Ti6Al4V dissimilar joints. *The International Journal of Advanced Manufacturing Technology*. 2017;92(9-12):3703–3714.
- [23] Steinbach I, Pezzolla F, Nestler B, Seeßelberg M, Prieler R, Schmitz GJ, et al. A phase field concept for multiphase systems. *Physica D: Nonlinear Phenomena*. 1996;94(3):135–147.
- [24] Qin R, Bhadeshia H. Phase field method. *Materials science and technology*. 2010;26(7):803–811.
- [25] Chen LQ. Phase-field models for microstructure evolution. *Annual review of materials research*. 2002;32(1):113–140.
- [26] Moelans N, Blanpain B, Wollants P. An introduction to phase-field modeling of microstructure evolution. *Calphad*. 2008;32(2):268–294.
- [27] Izyumov YA, Syromyatnikov VN. *Phase transitions and crystal symmetry*. vol. 38. Springer Science & Business Media; 2012.
- [28] Saunders N, Miodownik AP. *CALPHAD (calculation of phase diagrams): a comprehensive guide*. vol. 1. Elsevier; 1998.
- [29] Welland M, Piro M, Hibbins S, Wang N. A method of integrating CALPHAD data into phase-field models using an approximated minimiser applied to intermetallic layer growth in the Al-Mg system. *Calphad*. 2017;59:76–83.
- [30] Cahn J, Allen S. A microscopic theory for domain wall motion and its experimental verification in Fe-Al alloy domain growth kinetics. *Le Journal de Physique Colloques*. 1977;38(C7):C7–51.
- [31] Schmitz G, Böttger B, Eiken J, Apel M, Viardin A, Carré A, et al. Phase-field based simulation of microstructure evolution in technical alloy grades. *International Journal of Advances in Engineering Sciences and Applied Mathematics*. 2010;2(4):126–139.
- [32] Nomura Y, Minamoto S, Nomoto S. Simulations of solidification in Sn–3Ag–0.5 Cu alloys by the multi-phase-field method. *ISIJ international*. 2010;50(12):1920–1924.
- [33] Böttger B, Schmitz G, Santillana B. Multi-phase-field modeling of solidification in technical steel grades. *Transactions of the Indian Institute of Metals*. 2012;65(6):613–615.
- [34] Minamoto S, Nomoto S, Hamaya A, Horiuchi T, Miura S. Microstructure simulation for solidification of magnesium–zinc–yttrium alloy by multi-phase-field method coupled with CALPHAD database. *ISIJ international*. 2010;50(12):1914–1919.
- [35] Schaffnit P, Apel M, Steinbach I. Simulation of ideal grain growth using the multi-phase-field model. In: *Materials Science Forum*. vol. 558. Trans Tech Publications Ltd.; 2007. p. 1177–1181.
- [36] Apel M, Böttger B, Rudnizki J, Schaffnit P, Steinbach I. Grain growth simulations including particle pinning using the multiphase-field concept. *ISIJ international*. 2009;49(7):1024–1029.
- [37] Schneider D, Schoof E, Huang Y, Selzer M, Nestler B. Phase-field modeling of crack propagation in multiphase systems. *Computer Methods in Applied Mechanics and Engineering*. 2016;312:186–195.
- [38] Nguyen TT, Rethore J, Yvonnet J, Baietto MC. Multi-phase-field modeling of anisotropic crack propagation for polycrystalline materials. *Computational Mechanics*. 2017;60(2):289–314.
- [39] Steinbach I, Apel M. Multi phase field model for solid state transformation with elastic strain. *Physica D: Nonlinear Phenomena*. 2006;217(2):153–160.
- [40] Militzer M, Azizi-Alizamini H. Phase field modelling of austenite formation in low carbon steels. In: *Solid State Phenomena*. Trans Tech Publications Ltd.; 2011. .
- [41] Nakajima K, Apel M, Steinbach I. The role of carbon diffusion in ferrite on the kinetics of cooperative growth of pearlite: A multi-phase field study. *Acta Materialia*. 2006;54(14):3665–3672.
- [42] Zhang L, Steinbach I, Du Y. Phase-field simulation of diffusion couples in the Ni–Al system.

- International Journal of Materials Research. 2011;102(4):371–380.
- [43] Takaki T, Tomita Y. Static recrystallization simulations starting from predicted deformation microstructure by coupling multi-phase-field method and finite element method based on crystal plasticity. *International Journal of Mechanical Sciences*. 2010;52(2):320–328.
- [44] Park M, Gibbons S, Arróyave R. Phase-field simulations of intermetallic compound evolution in Cu/Sn solder joints under electromigration. *Acta Materialia*. 2013;61(19):7142–7154.
- [45] Park M, Gibbons S, Arroyave R. Phase-field simulations of intermetallic compound growth in Cu/Sn/Cu sandwich structure under transient liquid phase bonding conditions. *Acta Materialia*. 2012;60(18):6278–6287.
- [46] Park MS, Arroyave R. Formation and growth of intermetallic compound Cu₆Sn₅ at early stages in lead-free soldering. *Journal of electronic materials*. 2010;39(12):2574–2582.
- [47] Li J, Agyakwa P, Johnson C. Interfacial reaction in Cu/Sn/Cu system during the transient liquid phase soldering process. *Acta Materialia*. 2011;59(3):1198–1211.
- [48] Umantsev A. Modeling of intermediate phase growth. *Journal of applied physics*. 2007;101(2):024910.
- [49] Huh J, Hong K, Kim Y, Kim K. Phase field simulations of intermetallic compound growth during soldering reactions. *Journal of electronic materials*. 2004;33(10):1161–1170.
- [50] Hou H, Zhao Y, Zhao Y. Simulation of the precipitation process of ordered intermetallic compounds in binary and ternary Ni–Al-based alloys by the phase-field model. *Materials Science and Engineering: A*. 2009;499(1-2):204–207.
- [51] Wang Y, Banerjee D, Su C, Khachatryan A. Field kinetic model and computer simulation of precipitation of L12 ordered intermetallics from FCC solid solution. *Acta materialia*. 1998;46(9):2983–3001.
- [52] Plapp M. Unified derivation of phase-field models for alloy solidification from a grand-potential functional. *Physical Review E*. 2011;84(3):031601.
- [53] Steinbach I, Zhang L, Plapp M. Phase-field model with finite interface dissipation. *Acta Materialia*. 2012;60(6-7):2689–2701.
- [54] Steinbach I. Phase-field models in materials science. *Modelling and simulation in materials science and engineering*. 2009;17(7):073001.
- [55] Kim SG, Kim WT, Suzuki T, Ode M. Phase-field modeling of eutectic solidification. *Journal of crystal growth*. 2004;261(1):135–158.
- [56] Larché F. FC Larché and JW Cahn, *Acta Metall*. 33, 331 (1985). *Acta Metall*. 1985;33:331.
- [57] Steinbach I, Pezzolla F. A generalized field method for multiphase transformations using interface fields. *Physica D: Nonlinear Phenomena*. 1999;134(4):385–393.
- [58] Handbook A. vol. 1, 2 Metals handbook, vol. 3 Alloy phase diagram. ASM International, Materials Park Ohio, USA. 1992.
- [59] Jafarian M, Rizi MS, Jafarian M, Honarmand M, Javadinejad HR, Ghaheri A, et al. Effect of thermal tempering on microstructure and mechanical properties of Mg-AZ31/Al-6061 diffusion bonding. *Materials Science and Engineering: A*. 2016;666:372–379.
- [60] AFGHAHI SSS, Jafarian M, Paidar M, Jafarian M. Diffusion bonding of Al 7075 and Mg AZ31 alloys: Process parameters, microstructural analysis and mechanical properties. *Transactions of Nonferrous Metals Society of China*. 2016;26(7):1843–1851.
- [61] Zhong Y, Yang M, Liu ZK. Contribution of first-principles energetics to Al–Mg thermodynamic modeling. *Calphad*. 2005;29(4):303–311.
- [62] Murray JL. The Al-Mg (aluminum- magnesium) system. *Journal of Phase Equilibria*. 1982;3(1):60.
- [63] Saunders N. A review and thermodynamic assessment of the Al-Mg and Mg-Li systems. *Calphad*. 1990;14(1):61–70.
- [64] Zuo Y, Chang Y. Thermodynamic calculation of the Al-Mg phase diagram. *Calphad*. 1993;17(2):161–174.
- [65] Dinsdale A. SGTE data for pure elements. *Calphad*. 1991;15(4):317–425.
- [66] Hong K, Huh JY. Phase field simulations of morphological evolution and growth kinetics of solder

- reaction products. *Journal of electronic materials*. 2006;35(1):56–64.
- [67] Kim SG, Kim WT, Suzuki T. Phase-field model for binary alloys. *Physical review e*. 1999;60(6):7186.
- [68] Suhuddin U, Fischer V, Dos Santos J. The thermal cycle during the dissimilar friction spot welding of aluminum and magnesium alloy. *Scripta Materialia*. 2013;68(1):87–90.
- [69] Kim HS, Lee HJ, Yu YS, Won YS. Three-dimensional simulation of intermetallic compound layer growth in a binary alloy system. *Acta Materialia*. 2009;57(4):1254–1262.
- [70] Park M, Arróyave R. Multiphase field simulations of intermetallic compound growth during lead-free soldering. *Journal of electronic materials*. 2009;38(12):2525.
- [71] Brennan S, Bermudez K, Kulkarni NS, Sohn Y. Interdiffusion in the Mg-Al system and intrinsic diffusion in β -Mg₂Al₃. *Metallurgical and Materials Transactions A*. 2012;43(11):4043–4052.
- [72] Kulkarni KN, Luo AA. Interdiffusion and phase growth kinetics in magnesium-aluminum binary system. *Journal of phase equilibria and diffusion*. 2013;34(2):104–115.
- [73] Bellemans I, Moelans N, Verbeken K. Phase-field modelling in extractive metallurgy. *Critical Reviews in Solid State and Materials Sciences*. 2018;43(5):417–454.